INL/RPT-22-69625

Evaluation of Mechanistic and Empirical Models against Existing FFRD and LOCA Experimental Databases

September 30, 2022

Technical Report

Kyle A. Gamble[1], Ryan T. Sweet[1], Pierre-Clément A. Simon[1], Larry K. Aagesen[1], and Sudipta Biswas[1]

[1]Idaho National Laboratory

INL is a U.S. Department of Energy National Laboratory operated by Batelle Energy Alliance, LLC

Evaluation of Mechanistic and Empirical Models against Existing FFRD and LOCA Experimental Databases

Technical Report

Kyle A. Gamble[1], Ryan T. Sweet[1], Pierre-Clément A. Simon[1], Larry K. Aagesen[1], and Sudipta Biswas[1]

[1]Idaho National Laboratory

September 30, 2022

Idaho National Laboratory
Computational Mechanics and Materials Department
Idaho Falls, Idaho 83415

http://www.inl.gov

Prepared for the
U.S. Department of Energy
Office of Nuclear Energy
Under U.S. Department of Energy-Idaho Operations Office
Contract DE-AC07-05ID14517

Page intentionally left blank

Abstract

The desire of the nuclear industry to improve the economics of existing nuclear power plants has necessitated research into the potential of a phenomenon known as fuel fragmentation, relocation, and dispersal (FFRD). This phenomenon is possible during a loss-of-coolant accident (LOCA) at relatively high burnup. The Nuclear Energy Advanced Modeling and Simulation program has been developing simulation capabilities for FFRD and LOCA in the BISON fuel performance code for multiple years. This year, the effort has been focused on evaluating new lower length scale informed pulverization thresholds as well as updating and adding new empirical models for various phenomena. Models added or updated this year include a preliminary transient fission gas release model, new high-temperature Zircaloy creep models, a Zircaloy rupture opening area model, and a temperature-dependent emissivity during radiation from the fuel rod to the surrounding atmosphere. The models are verified through implementation tests to demonstrate code correctness after addition to BISON. The models are then assessed against a subset of the existing BISON validation suite for LOCA and FFRD cases. Two new cases, Studsvik Rods 192 and 193, have been added. The results indicate that the inclusion of a bubble pressure evolution model in the bubbles in the high-burnup structure has the largest impact compared to the 3D fracture criterion on reducing the calculated amount of pulverized fuel.

Page intentionally left blank

Contents

List of Figures

List of Tables

1. Introduction

The nuclear industry is actively pursuing higher discharge burnups of fuel rods in light-water reactors past the current regulatory limit of 62 MWd/kgU up to 75 MWd/kgU. The increase in burnup results in the potential of fuel fragmentation, relocation, and dispersal (FFRD) during a loss-of-coolant accident (LOCA). Fine fragmentation of the high burnup structure (HBS) accompanied with cladding distention due to the degradation of the heat transfer coefficient resulting from the coolant lost can lead to a redistribution of the fuel throughout the rod. Typically, a large portion of the fuel will accumulate in the ballooned region of the rod, which is also the location where the cladding is likely to rupture (fail). A comparison of the rupture area compared to the size of the fuel particles present will determine the likelihood of fuel dispersal into the primary coolant system. The nuclear industry must demonstrate methodologies to preclude fuel dispersal from occurring or to mitigate the impacts associated with the dispersion of fuel particles throughout the primary coolant system.

For many years, the United Stated Department of Energy Nuclear Engineering Advanced Modeling and Simulation program has developed simulation capabilities to gain an improved understanding into the behavior of fuel rods during a LOCA. In particular, a multiscale modeling approach has been used to develop a new pulverization threshold for UO_2 that accounts for the underlying material behavior associated with fission gas bubble pressure in the HBS as well as the fracture strength of the HBS. The new pulverization threshold has been implemented into the BISON [1] fuel performance code. In addition, a preliminary transient fission gas release model and lower-length scale informed recrystallization fraction (HBS formation) model have been added to BISON. Two new empirical options for high-temperature cladding creep have been made available, as well as two empirical options for predicting the size of the rupture opening in burst cladding tubes.

This report provides a summary of the latest improvements to empirical and mechanistic models for LOCA behavior added to BISON. The models are then verified via a set of regression tests that demonstrate the correct implementation in the code. The report continues with an assessment of the impact of the models to a variety of separate effects and integral rod tests from the BISON test suite. The majority of these cases have been added in previous years and are revisited to compare the impact of the new models. Two new cases from the Nuclear Regulatory Commission sponsored Studsvik LOCA tests Rods 192 and 193. This work concludes with a summary of the findings of the BISON studies using both the new mechanistic and empirical models with an outlook on future work.

2. Model Development

Both mechanistic and empirical models are used in the verification and validation studies completed in this work. This chapter presents both updates to existing and new models. Models addressing both fuel and cladding behavior have been improved or added, including an updated lower-length scale informed pulverization criterion, a preliminary transient fission gas release model, a lower-length scale informed recrystallization fraction model, new empirical options for high-temperature cladding creep, and two empirical options for predicting the size of the rupture opening in burst cladding tubes. Updates have also been made to the hydrogen embrittlement and damage model implemented into BISON last year [2].

2.1 Pulverization Criterion

2.1.1 Analytical Criterion for Pulverization

For completeness, the analytical model implemented last year is presented as it is used to show the impact of the changes in the phase-field criterion in some of the assessment and validation cases. The analytical criterion for pulverization is based on an expression that was originally developed for fragmentation along grain boundaries for lenticular bubbles in UO_2 [3]. Because pulverization predominantly occurs in regions where the high burnup structure (HBS) in UO_2 fuel has formed, the analytical model has been adapted to apply to the morphology of bubbles in the HBS region. These bubbles are approximately spherical and their sizes can be described by a log-normal distribution. The criterion for fine fragmentation to occur is met when the gas pressure P_g inside the statistically most common bubble (i.e., the bubble with the statistically most common size) exceeds the critical pressure P_g^{cr}:

$$P_g^{cr} = \frac{2\gamma}{r} + \frac{\sigma_{gb}^{cr}(1-\phi_2) - \sigma_H}{\phi_2} \tag{2.1}$$

where γ is the surface tension of the bubble-fuel interface, r is the bubble radius, σ_{gb}^{cr} is the critical fracture stress of the grain boundaries intersecting the bubble, ϕ_2 is a real fraction of the grain boundary occupied by the bubble, and σ_H is the local hydrostatic stress. In applying this equation, we assumed that there is a uniform array of the statistically most likely bubbles and that a flat grain boundary intersects each bubble; this neglects the more complex actual morphology of the bubbles and of the grain boundaries in the HBS. The statistically most common bubble size is $r \approx 0.5$ μm [4]. Additionally, it is assumed that the local volume fraction of HBS formation must be greater than a threshold value (user definable with a default of 0.5) for pulverization to occur.

Given the assumed geometry, ϕ_2 can be calculated from the local porosity in the HBS structure, p, using:

$$\phi_2 = \left(\frac{3p\sqrt{\pi}}{4}\right)^{2/3} \tag{2.2}$$

2.1.2 Phase-Field Fracture Criterion for Pulverization

The criterion for fine fragmentation to occur is met when the gas pressure P_g inside the statistically most common bubble (i.e., bubble with the statistically most common size) exceeds the critical pressure P_g^{cr}. This critical pressure is determined based upon phase-field fracture simulations of fragmentation of a pressurized gas bubble in the HBS region. The grain structure is assumed to be fully restructured with an average grain size of 200 nm. The most common bubble size of $r = 0.5$ μm was used in a phase-field fracture model with periodic boundary conditions. The domain size, external pressure, and critical fracture stress of the grain boundary were varied in the simulations. Two different equations exist for P_g^{cr} depending upon the dimension of the underlying phase-field simulations (2D or 3D). Choosing between the correlations is controlled by the parameter `fracture_criterion_3D` with a value of false for 2D and true for 3D. The following equation for P_g^{cr} in Pa was fit to the 2D data [5]:

$$P_g^{cr} = 1.0 \times 10^6 \left[\left(124.17 + 1.43858 \left(\sigma_{gb}^{cr} - 130 \right) \right) (1 - p) - 1.0178 \sigma_H \right] \tag{2.3}$$

where σ_{gb}^{cr} and σ_H are in MPa. For the 3D data, the equation of P_g^{cr} in Pa becomes [6]:

$$P_g^{cr} = 1.0 \times 10^6 \left[\left(175.987 + 0.5035 \left(\sigma_{gb}^{cr} - 130 \right) \right) (1 - 1.582 p) - 1.089 \sigma_H \right] \tag{2.4}$$

It is important to note that References [5, 6] refer to external pressure (P_{ext}) when defining the equations for P_g^{cr}. Equation 2.3 and Equation 2.4 use the definition of $P_{ext} = -\sigma_H$. Again, it is assumed that the local volume fraction of HBS formation must be greater than a threshold value (user definable with a default of 0.5) for pulverization to occur.

2.1.3 Bubble Pressure Calculation

Previously, the bubble pressure of the gas in the statistically most likely bubble was assumed constant with a default value of 100 MPa at 673 K [5]. Now the evolution of the pressure in the bubble and the size of the bubble can now computed based on the following set of equations by setting (`evolve_bubble_pressure = true`) in the input. A value of `false` will resort to a user-input approach. The gas concentration in the solid matrix surrounding the bubbles is assumed to be in quasi-steady-state conditions. In this case, the number of gas atoms transported to each existing bubble is equal to the production rate per unit volume, divided by the number of bubbles per unit volume:

$$\frac{d\bar{n}}{dt} = \frac{Y \dot{F}}{N}, \tag{2.5}$$

where $\bar{n}$ is the number of gas atoms per bubble, Y is the fission gas yield, $\dot{F}$ is the fission rate density, and N is the number of bubbles per unit volume. The number of vacancies per bubble, n_{iv}, was calculated as [7]:

$$\frac{dn_{iv}}{dt} = \frac{2\pi D_{ig}^v \rho}{kT\zeta} \left(P - P_{eq} \right), \tag{2.6}$$

where D_{ig}^v is the intra-granular vacancy diffusion coefficient, ρ is the radius of the equivalent Wigner-Seitz cell surrounding a bubble, and ζ is a dimensionless factor defined as:

$$\zeta = \frac{10\psi(1 + \psi^3)}{-\psi^6 + 5\psi^2 - 9\psi + 5}, \tag{2.7}$$

where $\psi = r/\rho$. P_{eq} is the equilibrium pressure for a bubble of radius r, as calculated using the Laplace-Young equation:

$$P_{eq} = \frac{2\gamma}{r} - \sigma_h, \tag{2.8}$$

After updated values of $\bar{n}$ and n_{iv} are calculated, the bubble pressure is calculated using a rearranged formulation of the van der Waals equation of state [7]:

$$P_g = \frac{kT}{\Omega}\frac{\bar{n}}{n_{iv}} \tag{2.9}$$

where $\Omega = 4.09 \times 10^{-29}$ m^3 is the volume of a vacancy on a U lattice site in UO_2. The updated bubble volume is calculated using:

$$V_b = \omega\bar{n} + \Omega n_{iv} \tag{2.10}$$

where $\omega = 8.5 \times 10^{-29}$ m^3 is the van der Waals atomic volume for Xe [8]. The current bubble radius is calculated from the volume as:

$$r = \sqrt[3]{\frac{3V_b}{4\pi}} \tag{2.11}$$

2.2 Transient Fission Gas Release Model

A new mechanistic model for transient fission gas release (tFGR) has been developed as part of Reference [6]. This model accounts for the amount of FGR due to fuel pulverization at high burnup. This is one of the mechanisms proposed to contribute to tFGR. The amount of FGR is calculated using the approach developed in Reference [6].

During fuel pulverization, a fraction of the pores become exposed to free surfaces and release fission gas. The amount of fission gas released is therefore equal to:

$$n_{tFG}^{pul} = f_V^{pul} n_{FG} V^{pul}, \tag{2.12}$$

where n_{FG} is the density of fission gas release in the pulverized fuel in moles/m^3, derived as the product of the bubble density in bubble/m^3 and the average number of atoms in intragranular gas bubbles (atoms/bubble), and divided by Avogadro's number. V^{pul} is the volume of pulverized fuel in m^3, and f_V^{pul} is the volume fraction of bubbles opened during fuel pulverization, over the total bubble volume.

f_V^{pul} is expected to depend on pore structure, fragment size, and porosity. Its derivation based on a geometric criteria is detailed in Reference [6] and illustrated in Fig. 2.1. Assuming cuboid fuel fragments of size l_f and homogeneous bubble radius r_b, f_V^{pul} is defined as:

$$f_V^{pul} = \frac{V_{b,open}^{pul}}{V_b^{pul}}, \tag{2.13}$$

where V_b^{pul} is the total bubble volume in pulverized fuel and $V_{b,open}^{pul}$ is the volume of pores that become exposed during fragmentation. Performing calculations on a number of random bubble microstructures showed that f_V^{pul} can be approximated as:

$$f_V^{pul} = c_p p + c_r \frac{r_b}{l_f} + c_0, \tag{2.14}$$

where $c_p = 0.03$ (-) is the coefficient for the porosity, $c_r = 5.17$ (-) is the coefficient for the bubble-radius-

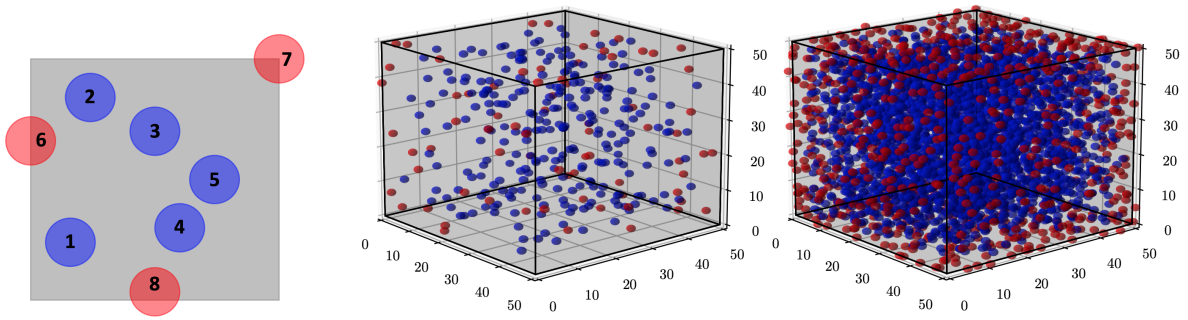

(a) 2D illustration

(b) $p = 1\%$, $r_b = 1$: $f_V^{pul} = 0.061$

(c) $p = 10\%$, $r_b = 1$: $f_V^{pul} = 0.122$

Figure 2.1. Illustration of the definition of $V_{b,open}^{pul}$ and f_V^{pul} and their importance in determining FGR during pulverization [6]. In (a), a 2D fragment is shown in light grey, and the bubbles with radius R are shown in blue and red, along with number labels. Bubbles 1–5 (blue) are completely contained in the fragment, and thus do not contribute to FGR. Their contribution to the total bubble volume is equal to $5 \times 4/3\pi R^3$. Their contribution to the open bubble volume is 0. However, Bubbles 6, 7, and 8 became exposed during pulverization. Their contribution to the total bubble volume is equal to $1/2 \times 4/3\pi R^3$, $1/4 \times 4/3\pi R^3$, and $3/4 \times 4/3\pi R^3$, respectively, as is their contribution to the open bubble volume. For this pore structure, $f_V^{pul} = 3/13 = 0.231$. (b) and (c) provide 3D examples of generated pore structures at different porosity levels p and bubble radii r_b, with the fragment size fixed at $l_f = 50$ μm [9, 10]. Pores completely contained in the fragment are shown in blue, whereas pores opened during pulverization (i.e., in contact with the fragment surface) are shown in red. For each pore structure, f_V^{pul} is provided. Note that due to the random nature of the algorithm, different f_V^{pul} can be obtained for the given porosity and bubble radius values.

to-fragment-size ratio, and $c_0 = 0.02$ (-) is a constant [6]. These values have been derived by generating hundreds of randomly distributed pore microstructures and computing the ratio of open bubble volume over the total bubble volume [6]. This correlation has been derived for a porosity ranging from 1 to 13% [11, 12, 13] and a bubble-radius-to-fragment-size ratio $\frac{r_b}{l_f}$ ranging from 0.01 to 0.1. These values are relevant for fragment sizes of tens of microns [9, 10] and bubble radii between 0.01 and 5 μm [14, 9, 10, 15, 16].

This new model has been added to BISON with the name `UO2PulverizationTransientFissionGasRelease`. It has been tested and verified, and the results are described in Chapter 3. Its impact on selected BISON assessment cases are discussed in Chapter 4.

2.3 Recrystallization Fraction

Determining the volume fraction of the restructured HBS fuel is important for evaluating the performance of the fuel after restructuring (i.e., the fission gas release behavior and pulverization criteria of the restructured fuel). Currently, BISON uses a semi-empirical correlation derived based on limited experimental data to predict the restructured volume fraction. A mesoscale model is currently under development in Marmot to simulate the HBS formation and associated fission gas evolution in UO_2 [17, 5, 6]. The mesoscale recrystallization model uses an effective burnup-dependent grain subdivision criteria, which nucleate new defect-free grains when the dislocation density of the damaged grains exceeds the critical value for recrystallization. The nucleation rate and average restructured grain size vary with the temperature [17]. In general, the HBS volume fraction can be calculated using the Kolmogorov-Johnson-Mehl-Avrami (KJMA) correlation

for phase transformations such that [7]:

$$\alpha = 1 - \exp\left(-k\, bu_{eff}^{n}\right) \tag{2.15}$$

where α is the volume fraction of the new grains, k is the transformation rate constant, bu_{eff} is the effective burnup, and n is the Avrami constant.

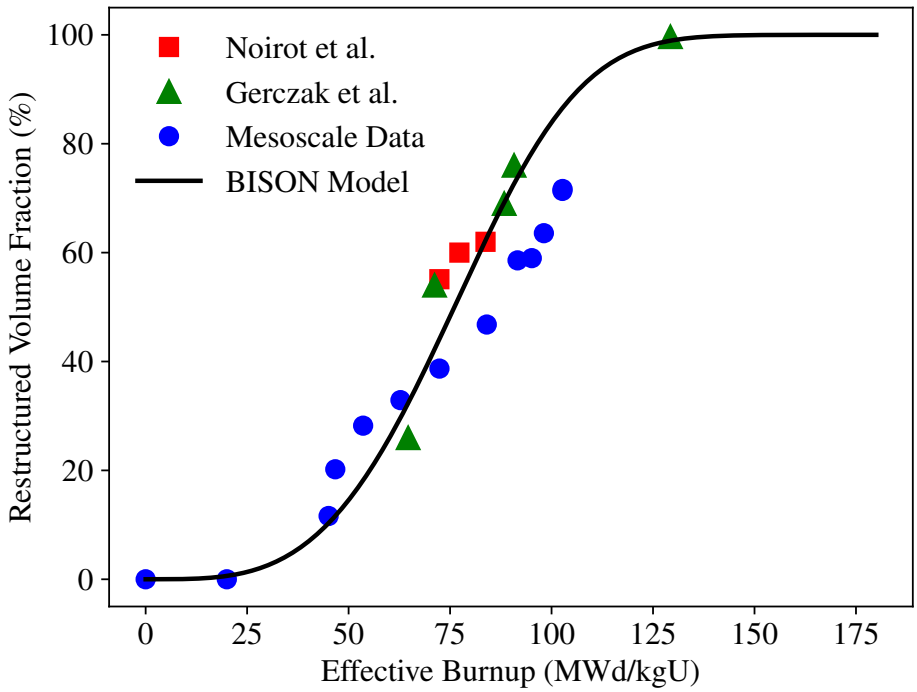

Figure 2.2. Variation of the volume fraction of the restructured HBS region with the effective burnup. The slope of the mesocale data varies from the current BISON model, indicating the need for an updated model.

Figure 2.2 compares the mesoscale data with the existing BISON model and experimental data used for fitting the said model. The mesoscale data follows the KJMA correlation. However, the slope of the curve is different from what the current BISON model uses. Moreover, the mesoscale simulations have shown that the time to achieve a complete restructuring could vary with temperature [18]. Thus, the slope of the model (k) should be a function of temperature. The mesoscale observations do not support the assumption of the current BISON model that the slope of the curve remains constant below a threshold temperature. Therefore, the BISON model needs to be updated based on lower-length scale data for a more accurate prediction of the HBS volume fraction in the fuel. This will be pursued in the future.

2.4 High-Temperature Zircaloy Creep

Accurate evaluation of the cladding deformation due to thermal creep is necessary to determine the cladding rupture behavior under high-temperature conditions, such as those encountered during a LOCA or cladding burst test. In addition to the existing Erbacher model [] in BISON, additional phase-dependant models available in the literature were implemented and evaluated [19, 20].

2.4.1 Kaddour Creep Model

The Kaddour model is similar in power-law creep rate form to the Erbacher model, however the prefactor of the creep strain now includes a temperature dependence. The effective creep strain rate ($\dot{\epsilon}_{eff}$) is given as:

$$\dot{\epsilon}_{eff} = \frac{A}{T} \exp\left(\frac{-Q}{RT}\right) {\sigma_{eff}}^n \tag{2.16}$$

where A (K MPa^{-n}s^{-1}) is the creep coefficient, Q (J/mol) is the activation energy for the creep deformation, T (K) is the temperature, σ_{eff} (MPa) is the effective (von Mises) stress, and n (-) is the stress exponent. Identically to the Erbacher model, the components of the strain tensor are then updated at each time step based on the effective strain increment and a flow rule. The material parameters, shown in Table 2.1, used in the model were obtained from tension tests on Zircaloy-4 tubes [21].

Table 2.1. Material parameters used to calculate the creep in Zircaloy-4 using the Kaddour model [21].

Phase	σ_{eff} (MPa)	A (K MPa^{-n} s^{-1})	Q (J/mol)	n (-)
Pure α phase	≤ 15	1.0×10^6	1.90×10^5	1.3
Pure α phase	> 15	1.63×10^8	3.16×10^5	5.00
Mixed: 50 % α phase, 50% β phase	all stresses	lin. interp. of ln (A)	lin. interp.	lin. interp.
Pure β phase	all stresses	1.0×10^4	1.50×10^5	4.25

A linear interpolation of ln(A), n, and Q is made between the values for mixed phases between the pure α and β phases [19]. If the fraction of β phase is more than 0, the higher stress α phase coefficients are used for the creep parameter interpolation for mixed phases.

2.4.2 Donaldson Creep Model

The Donaldson model is similar in power-law creep rate form to the Kaddour and Erbacher models; however, the prefactor of the creep strain includes both the temperature-dependant shear modulus and the temperature, while the stress is divided by the shear modulus. It leads to:

$$\dot{\epsilon}_{eff} = \frac{AG(T)}{T} \exp\left(\frac{-Q}{RT}\right) \left(\frac{\sigma_{eff}}{G}\right)^n \tag{2.17}$$

where $\dot{\epsilon}_{eff}$ (s^{-1}) is the effective creep strain rate, A (K-MPa^{-n}s^{-1}) is the creep coefficient, Q (J/mol) is the activation energy for the creep deformation, T (K) is the temperature, G (MPa) is the shear modulus, σ_{eff} (MPa) is the effective (von Mises) stress, and n (-) is the stress exponent. The shear modulus is computed as:

$$G(T) = 3.326 \times 10^4 - 2.244 \times 10^1 (T - 273.15) + 2.161 \times 10^{-3} (T - 273.15)^2 \tag{2.18}$$

where G is the shear modulus (MPa) and T is the temperature in K.

Identically to the Erbacher model, the components of the strain tensor are then updated at each time step based on the effective strain increment and a flow rule. The material parameters, shown in Table 2.2, used in the model were obtained from isothermal, internally pressurized tube tests using Zircaloy-4 tubes [22]. The Donaldson model is derived using radial deformation data, which allows the calculated creep coefficients A_{hoop} to be converted into the axial direction A_z using the Hill model. In this model, an option is provided to select the direction to be used. Because of the specificity of this model, it is more appropriate to use the Hoop option when evaluating the cladding hoop strain and failure based on the hoop strain.

Table 2.2. Material parameters used to calculate the creep in Zircaloy-4 using the Donaldson model [22, 20]

Phase	A_z (MPa^{-n} s^{-1})	A_{hoop} (MPa^{-n} s^{-1})	Q (J/mol)	n (-)
Pure α phase	4.55×10^{23}	4.43×10^{22}	2.668×10^5	5.31
Mixed: 50% α phase, 50% β phase	5.50×10^{10}	1.966×10^5	1.966×10^5	1.89
Mixed: 50% α phase, 50% β phase	lin. interp. of ln (A)	lin. interp. of ln (A)	lin. interp.	lin. interp.
Pure β phase	2.92×10^{13}	1.49×10^{13}	$.93 \times 10^5$	3.68

Linear interpolation of ln(A), n, and Q is made between the values for pure α and the equally mixed phases of $\alpha + \beta$ (50%α–50%β), and between 50%α-50%β and pure β phases [22, 19].

2.5 Hydrogen Embrittlement and Damage

The model for hydrogen embrittlement and damage implemented into BISON last year [2] has been extended to work in conjunction with normal and high-temperature creep models. The model has also been improved by obtaining the matrix (Zircaloy) mechanical properties (i.e., Young's modulus and Poisson's ratio) from the elasticity tensor rather than requiring user input. These changes improve consistency amongst all Zircaloy models when using the hydrogen embrittlement and damage model and enables the ability to include the the model in LOCA analyses. The original theory behind the model is provided in detail in Reference [2].

2.6 Cladding Rupture Area

Over the last few years, a couple of empirical models have been proposed to estimate the rupture size in failed cladding tubes based upon quantities measured after the conclusion of experiments. Jernkvist [23] provided a comprehensive review of rupture opening measurements and developed a model based upon 235 tests. The report discusses the potential effects of hydrogen content on burst times through the modification of the α to $\alpha + \beta$ and β to $\alpha + \beta$ transition temperatures. In BISON, the Zircaloy phase is calculated by the `ZrPhase` model. According to Jernkvist, for fuel dispersal calculations, only the rupture opening width is important and not the rupture length. Thus, a model of the following form was proposed for the rupture width:

$$w_b\left(\sigma_b\right) = \alpha D_o\left(1 - \exp\left(-\beta\left(\sigma_b - \sigma_{th}\right)\right)\right) \tag{2.19}$$

where w_b is the rupture width (mm), D_o is the as-fabricated cladding diameter (mm), σ_b is the hoop stress at burst (MPa), and α, β, and σ_{th} are fitting constants. Best-estimate values of these constants were found to be $\alpha = 0.5848$, $\beta = 3.35 \times 10^{-8}$ Pa^{-1}, and $\sigma_{th} = 5$MPa. The correlation used to relate rupture opening area and rupture opening width is given by:

$$A_b = 0.619 w_b^2 \left(\frac{11.4}{w_b + 0.81} + 0.95\right) \tag{2.20}$$

where A_b is the rupture opening area (mm^2). This best-estimated model is said to bound 56.8% of the 285 supporting databases. A more conservative model can be captured by increasing the value of the constant α.

Once the rupture width has been determined, the area can be calculated by Equation 2.20 and the rupture length can be obtained by:

$$l_b = \frac{11.4 w_b}{w_b + 0.81} + 0.95 \tag{2.21}$$

The second empirical model for rupture area is based upon research conducted by a group at Oak Ridge National Laboratory (ORNL) [24]. The authors present two models that are denoted as the average and limiting models. The average model fits to most of the available experimental data depending upon the rupture opening shape chosen. The limiting case is more conservative and encompasses the majority of the available data, including outliers. The ORNL formulation is based on the peak cladding hoop strain at burst (%), which occurs at the burst location. The rupture length (mm) is estimated by:

$$l_b = C_1 \left(\epsilon_{hoop} - C_2\right)^{C_3} - C_4 \tag{2.22}$$

where ϵ_{hoop} is the peak cladding hoop strain (%) and C_1 (mm/%), C_2 (%), C_3(-), and C_4 (mm) are fitted constants. Depending upon whether the model is assumed to be average or limiting the constants are different. The determined coefficients for the two models are summarized in Table 2.3.

Table 2.3. Coefficients for the limiting and average models for rupture length by ORNL [24].

Model	C_1 (mm/%)	C_2 (%)	C_3 (-)	C_4 (mm)
Limiting	20	8	0.22	18
Average	55	8	0.09	60

Once the rupture length is estimated, the proposed correlations for the rupture width is given by:

$$w_b = \begin{cases} D_o \left(C_5 l_b^{C_6} + C_7\right), & l_b < l_{th} \\ D_o, & l_b \geq l_{th} \end{cases} \tag{2.23}$$

where D_o is the as-fabricated cladding outer diameter (mm), l_b is the rupture width, and C_5 (-), C_6 (-), C_7 (mm), and l_{th} are constants. The coefficients for the limiting and average cases for the rupture width are provided in Table 2.4.

Table 2.4. Coefficients for the limiting and average models for rupture width by ORNL [24].

Model	C_5 (-)	C_6 (-)	C_7 (mm)	l_{th} (mm)
Limiting	0.055	0.92	-0.01	24
Average	0.032	0.92	0	43

After defining the equations for the rupture length and width, Capps et al. [24] explored the rupture area calculated by assuming different rupture shapes: rectangle, rhombus, and ellipse (oval). The standard area equations for these primitive shapes are:

$$\text{Rectangle: } A_b = w_b l_b \tag{2.24a}$$

$$\text{Rhombus: } A_b = \frac{w_b l_b}{2} \tag{2.24b}$$

$$\text{Ellipse: } A_b = \frac{\pi w_b l_b}{4} \tag{2.24c}$$

2.7 Temperature-Dependent Emissivity for Radiation

Recent studies by Gamble [25] identified through a sensitivity analysis that the effective emissivity for radiation between the outer surface of the cladding and environment surrounding the fuel rods is the most influential parameter on the cladding distention and fuel relocation behavior. The ranges explored on the emissivity value ranged from 0.3 to 0.75, which are the minimum and maximum values obtained by the correlation proposed by Stuckert et al. [26] for the effective emissivity between Zircaloy and the core structure components. In simulated LOCA tests at Halden, heat can also be transferred to the heating element after blowdown. Radiation heat transfer is described by:

$$h_r = \epsilon\sigma(T_c^2 + T_s^2)(T_c + T_s) \tag{2.25}$$

where T_c is the cladding temperature and T_s is the environmental surface temperature (e.g., a heater), with ϵ given by:

$$\epsilon = \epsilon_c\epsilon_h R_h(\epsilon_c R_c + \epsilon_h R_h - \epsilon_c\epsilon_h R_c)^{-1} \tag{2.26}$$

where ϵ_c and ϵ_h are the surface emissivities of the cladding and heater, respectively, R_c and R_h are the radii of the two surfaces, and σ is the Stefan-Boltzmann constant (5.6704×10^{-8} W/m^2-K^4). The default value for the effective emissivity (ϵ) is 0.75, which is the upper limit. The user can provide a different value for the effective emissivity and use a constant value throughout the simulation. This year, the temperature-dependent correlation proposed by Stuckert et al. [26] has been added to BISON and can be enabled by the user by setting the `compute_effective_emissivity` option to true (default is false). If true, the user defined constant value is ignored and Equation 2.26 is computed by:

$$\begin{aligned}\epsilon\left(T\right) = p_0 + \frac{p_1 - p_0}{2}\left(\tanh\left(\frac{T - p_2}{p_3}\right) + 1\right) + \left(p_4 - p_1\right)\exp\left[-\left(\frac{T - p_2}{p_3}\right)^2\right] \\ - \left(p_5 - p_6\right)\exp\left[-\left(\frac{T - p_7}{p_8}\right)^2\right]\end{aligned} \tag{2.27}$$

where T is the temperature (K) and p_0–p_8 are numerically determined constants through statistical fitting. The value of these constants are tabulated in Table 2.5.

Table 2.5. Coefficients for the effective emissivity for radiation correlation [26].

$\mathbf{p}_0$	$\mathbf{p}_1$	$\mathbf{p}_2$	$\mathbf{p}_3$	$\mathbf{p}_4$	$\mathbf{p}_5$	$\mathbf{p}_6$	$\mathbf{p}_7$	$\mathbf{p}_8$
0.25505	0.31783	1184.78	34.5649	0.76264	0.19449	0.10137	1063.73	62.0845

3. Implementation Testing

In this chapter, demonstration cases for the new models introduced in Chapter 2 are presented to ensure that the code has been properly implemented and is computing the correct values. Tests of this type are added to the BISON code to prevent future code changes from causing a regression or change in the behavior of existing code. If changes do occur, a thorough understanding of those changes is required prior to updating the tests and adding the new version of the code. An example of where the tests were updated due to changes in model form as part of this work is the bubble evolution and 3D phase-field informed criterion used in the new pulverization threshold.

3.1 Pulverization Criterion

The pulverization criterion determines whether a material point in a BISON mesh has pulverized. Therefore, the calculation returns a Boolean value of either false (0) when a material has not yet pulverized or a value of true (1) when the material has pulverized. A volume integral over the entire fuel enables the computation of the volume of pulverized fuel, which in turn can be used to determine the mass of fuel pulverized using the as-fabricated density. The lower length scale (LLS) analytical and phase-field models are functions of the porosity in the HBS as well as recrystallization (or HBS) volume fraction. If the HBS fraction is greater than 0.5 and the bubble pressure exceeds the critical bubble pressure, pulverization is permitted to occur. The models for determining the HBS volume fraction and porosity in the HBS were previously implemented in BISON [27] and have already been verified to be implemented correctly. Therefore, in the tests for the pulverization criterion, it is assumed that the computation of the HBS volume fraction and porosity in the HBS is correct, and those values are simply used in the studies here.

To demonstrate the proper implementation of the pulverization threshold, the following geometry and conditions are used. The geometry of this test case is the same regardless of the fracture criterion employed. A Layered1D (or 1.5D) approach is used, consisting of five axial fuel slides without cladding. The outer fuel radius is 4.5 mm, and each slice has a height of 0.1 m. The burnup increases linearly from the fuel centerline to the fuel surface. The temperature is held constant at a value of $T = 673.15$ K from $t = 0$ s to $t = 100$ s, followed by a ramp in temperature from $t = 100$ s to $t = 110$ s at a rate of 15.5 K/s for the 2D fracture criterion. For the 3D fracture criterion, the temperature ramp rate is the same but the duration is extended to $t = 125$ s to reach a higher temperature to induce pulverization. Pulverization will only occur during the ramp, in the rim region where a significant amount of high-burnup structure formation has begun. The test is designed so that, in both cases, the three outermost elements in each layer pulverizes. Analytically, the volume of pulverized fuel in each layer is determined by:

$$V_p = \pi L \left(R_o^2 - R_p^2\right) \tag{3.1}$$

where L is the layer height (0.1 m), R_o is the outer fuel radius (4.5 mm), and R_p is the radius into the fuel at which point pulverization ends ($0.7R_o = 3.15$ mm). Substituting the known values into Equation 3.1 results

in a pulverized fuel volume of 3.24448×10^{-6} m^3 in each layer. Line plots for the evaluation of the layered pulverized fuel volume for both the 2D and 3D phase field fracture criteria are illustrated in Figure 3.1. As can be seen, the layered pulverized volume in each layer is equal to the analytical solution at the end of the simulation in each case.

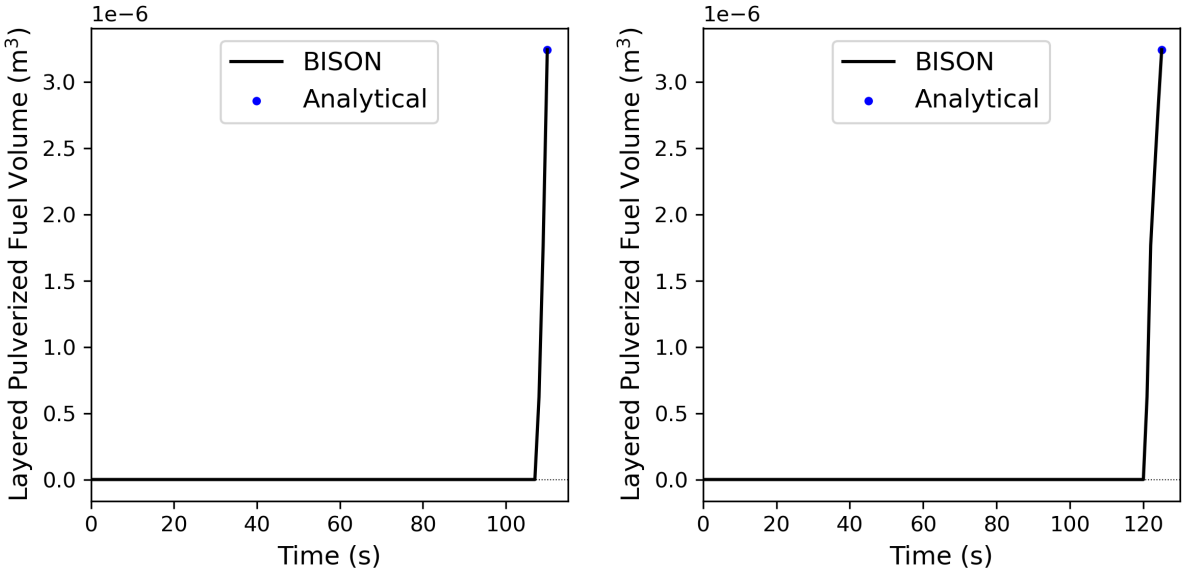

(a) (b)

Figure 3.1. Layered pulverized fuel volume as a function of time for the regression test using the pulverization criterion based upon (a) 2D and (b) 3D phase-field simulations.

3.2 Transient Fission Gas Release Model

The transient fission gas release model presented in Section 2.2 has been tested and verified as part of its implementation in BISON. The first series of tests check that a warning is returned in case f_V^{pul} (i.e., the volume fraction of bubbles opened during fuel pulverization over the total bubble volume), is not contained between 0 and 1. This could potentially happen during solve iterations and would lead to non-physical results. If f_V^{pul} is outside of [0,1], BISON returns a warning and it is set equal to the closest bound.

Another test verifies that, in the hypothetical case where the fuel is fully pulverized and the bubble size is greater than the fragment size (i.e., they are all on a free surface after pulverization), f_V^{pul} is equal to 1 and the amount of transient fission gas released due to pulverization n_{tFG}^{pul} is equal to the total amount of fission gas present in the bubbles n_{FG}. This ensures that n_{tFG}^{pul} could be equal to, but never exceeds, n_{FG}.

While the tests described above check the model in extreme, hypothetical scenarios, another test compares the BISON-predicted value against analytical calculations to verify its implementation. This test is built upon the existing pulverization test described in Section 3.1 for which the end time was $t = 125$ s. Here, a material property uses the local pulverization to compute the amount of fission gas released as a results of fuel pulverization. At each time step, the pulverized material property is computed, as well as the bubble radius and amount of fission gas in the bubbles. These material properties are then used to determine the

amount of fission gas release due to pulverization. This amount predicted by the the model implemented in BISON is compared with the analytical equation for verification. The successful comparison between BISON predictions and the analytical equation is shown in Fig. 3.2.

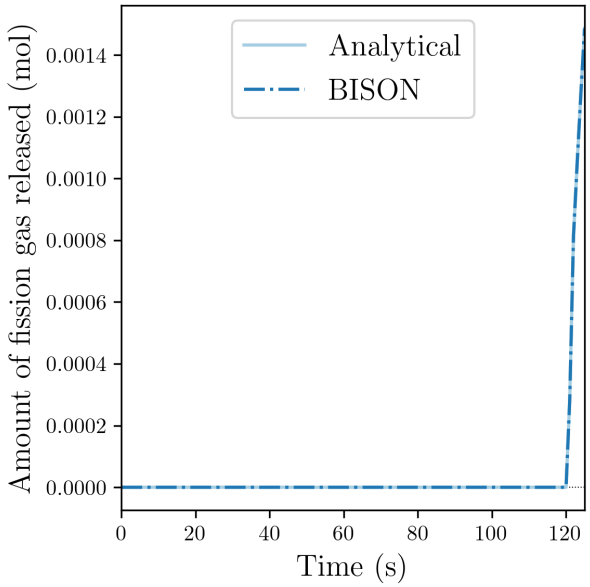

Figure 3.2. Verification results. The BISON predictions for the amount of tFGR due to pulverization exactly match the analytical calculations.

3.3 High-Temperature Zircaloy Creep

Creep rate contours generated using uniaxial tension tests are shown in Section 3.3 as a function of temperature and stress. The interpolation of creep parameters for the onset of the LOCA creep model (900 K) and the mixed phase of $\alpha + \beta$ for the cladding material is illustrated through distinct regions of the creep rate. The fraction of each phase is calculated by a separate model in BISON.

All three axial creep rate contours (Figure 3.3a, Figure 3.3b, and Figure 3.3d) show nearly identical behavior below 900 K due to the interpolation with the thermal creep model for normal operating temperature ranges. The magnitude of these axial creep rate models is very similar; however, due to the interpolation between specific regimes of each model, there are different features (i.e., the increase in creep rates for the different Donaldson directions [Figure 3.3c and Figure 3.3d] at 1150 K).

For the Kaddour model, Fig. 3.3a, the transition stress at 15 MPa in the pure α region is illustrated at ~900–1050 K. From this point, the model shows a relatively consistent interpolation for the creep-rate parameters based on temperature, resulting in more uniform contour shapes.

For the Donaldson model, two creep directions are considered, the hoop direction (Figure 3.3d) and the axial direction (Figure 3.3d). As previously discussed, the creep prefactor for the hoop direction is nearly an order of magnitude lower than the axial direction, which correspondingly reduced the creep rate. As the temperature increases to ~1150 K, the interpolation between the pure α and the $50\%\alpha - 50\%\beta$ region shows a slight decrease in the creep rate. Data from this model is needed to confirm this behavior; although, the

Erbacher model, Figure 3.3b, shows similar behavior (although not quite as exaggerated) due to the same phase interpolation at the same temperature.

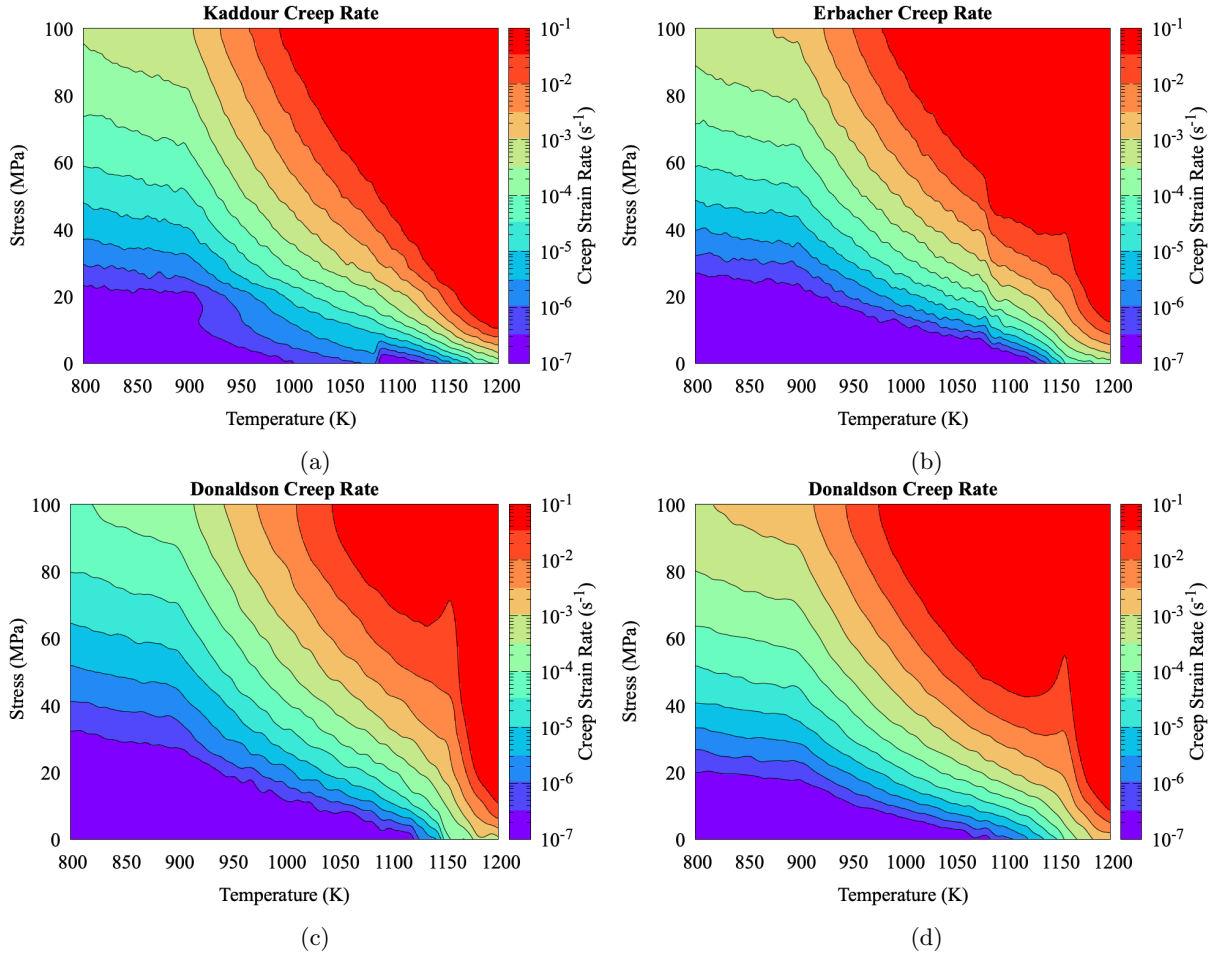

Figure 3.3. Creep strain rate contours for the (a) Kaddour, (b) Erbacher, (c) Donaldson (hoop), and (d) Donaldson (axial) models as a function of temperature and stress generated using uniaxial tension tests.

3.4 Hydrogen Embrittlement and Damage

Testing of the hydrogen embrittlement and damage mode is not trivial. The algorithm for the model described in Reference [2] highlights the fact that the evolution of the stress when using the model depends strongly on the concentration and orientation of the hydrides involving numerous loops to converge the solution on multiple material planes. In previous work [2], demonstration cases verified that the algorithm behaves correctly using a set of elementary studies, including a so-called patch test, rotation test, axisymmetric test, tensile test, and shear test. In many of these previous tests, the orientation of the hydrides and their concentration was fixed or the properties of the underlying matrix (i.e., Zircaloy) and hydrides were set equal to one another to verify the proper collapse of the algorithms to standard elastic and elastic-plastic

behavior. In this work, an existing normal operating temperature creep test for Zircaloy is used and hydrides and damage are introduced.

The following setup is considered for this test: a single axisymmetric finite element with a height of 0.01 m and inner and outer radii of 0.005 and 0.0055 m, respectively, is held at a constant temperature of 650 K. A 40-MPa pressure is applied on the inner surface with displacements constrained at the top and bottom of the element to simulate an infinitely long tube. The creep rate correlation is that of Limbäck and Anderson [28], which has been available in BISON for many years. The elastic properties of the hydrides are assumed to be $E = 96.7$ GPa and $\nu = 0.389$ with a volume fraction in the radial and circumferential directions of 0.005 and 0.067, respectively. Table 3.1 presents the creep strain in the radial, hoop, and axial directions. As can be seen, the creep strain is reduced in all directions due to the impact of the embrittlement and damage on the tube stress state. However, for these conditions, the differences are small.

Table 3.1. Comparisons between thermal creep rates with and without hydrides and damage.

	ϵ_{radial} (-)	ϵ_{hoop} (-)	ϵ_{axial} (-)
Without hydrides and damage	-1.093952 $\times 10^{-4}$	1.390169 $\times 10^{-4}$	-2.962168 $\times 10^{-5}$
With hydrides and damage	-1.082265 $\times 10^{-4}$	1.373868 $\times 10^{-4}$	-2.916024 $\times 10^{-5}$

3.5 Cladding Rupture Area

Implementation testing of the empirical rupture area model is designed to verify that the calculation of the rupture area for the three different models, Jernkvist, ORNL average, and ORNL limiting, are accurately computed using the peak cladding hoop strain or peak cladding hoop stress as appropriate given a specific loading scenario. For this demonstration, a cladding tube with an inner and outer radius of 0.005 and 0.0055 m, respectively, is subjected to a pressure linearly increased on the interior surface of the tube up to a maximum of 11 MPa at 11 seconds. The simulation is terminated when the peak hoop stress exceeds 100 MPa. In the ORNL studies, the Young's modulus was assumed to be 0.2 GPa, whereas, for the Jernkvist study, the value was set to 1 GPa. These values only affect the time the limiting stress is achieved as well as the peak cladding hoop strain at the time of termination. For the ORNL case, the simulation was terminated at a peak cladding hoop strain of 55.3 %. Using the equations in Section 2.6, one can compute the area for assumed oval, rectangle, and rhombus shapes for both the average and limiting cases. The calculated areas for this peak cladding hoop strain for the ORNL average and limiting models from BISON are shown in Table 3.2. For the Jernkvist study, the peak hoop stress at termination is 111.66 MPa. Using this value, the calculated opening area is 62.05 mm^2.

Table 3.2. BISON calculated rupture areas using the ORNL average and limiting models assuming rupture oval, rhombus, and rectangle shapes.

Model	Shape	Area (mm^2)
Average	Oval	69.8
Average	Rectangle	88.8
Average	Rhombus	44.4
Limiting	Oval	248.2
Limiting	Rectangle	316.0
Limiting	Rhombus	158.0

3.6 Temperature-Dependent Emissivity for Radiation

Demonstration of the temperature-dependent emissivity for radiation uses the following simple test. A 2D-RZ axisymmetric piece of cladding is held at an initial temperature of 600 K. The coolant temperature is also set to 600 K. Over 50 seconds, the heat flux is increased linearly from 0 to 132,000 W/m^2 on the inner surface of the cladding. The outer heat flux can be readily computed from using the thermal properties of the tube ($k = 16.0$ W/m-K). Once the heat flux at the outer surface is known, the temperature at the outer cladding surface (T_w) can be computed via:

$$T_w = \sqrt{\sqrt{\frac{q}{\sigma_b \epsilon_{eff}} + T_{coolant}^4}} \tag{3.2}$$

where σ_b is the Stefan-Boltzmann constant, ϵ_{eff} is the effective emissivity, and $T_{coolant}$ is the coolant temperature. Table 3.3 presents the results of the study.

Table 3.3. BISON- calculated wall temperatures for the demonstration case for the temperature-dependent emissivity.

Time (s)	Outer Heat Flux (W/m^2)	Emissivity (-)	BISON T_w (K)	Analytical T_w (K)
5	458.96	0.2551	633.77	633.77
10	2,023.13	0.2551	720.51	720.51
15	5,748.85	0.2550	852.08	852.08
20	10,791.43	0.2030	1016.38	1016.38
25	48,513.88	0.5111	1158.86	1158.86
30	69,580.21	0.6892	1175.61	1175.61
35	75,024.59	0.6876	1197.16	1197.16
40	63,595.65	0.3178	1383.02	1383.02
45	88,665.65	0.3178	1499.05	1499.05
50	107,405.46	0.3178	1570.90	1570.90

4. Assessment and Validation

Assessing the impact of various models on simulation predictions is of great importance. To this end, a series of experiments have been revisited from the BISON assessment and validation suite to evaluate the impact of different models on the fuel performance metrics of interest. Where available, comparisons to experimental data are provided to assess the validity of the simulation calculations. The types of experiments analyzed are broken into two separate areas: separate effects and integral rods. In separate effects experiments, the focus is on one particular phenomenon of interest (e.g., time to burst), whereas, for integral rod tests, many different phenomena (e.g., plenum pressure, fission gas release) are measured either online or after the conclusion of the experiment.

4.1 Separate Effects Experiments

4.1.1 REBEKA

The REBEKA separate effects tests [29, 30] are temperature transient tests in steam performed on single pressurized-water reactor size Zircaloy-4 tubes. The tests were to establish data on cladding ballooning and burst with reference to LOCA-like conditions. The cladding tubes had a fabricated inner and outer diameter of 9.30 and 10.75 mm, respectively, with a 325-mm heated length. The cladding was heated indirectly by conduction heating from the inside using an electrically insulated heater rod. The test parameters covered 1–14 MPa for the internal rod pressure and 1–30 K/s for the heating rate. The test atmosphere was almost stagnant steam at atmospheric pressure and 473 K. The cladding temperatures were measured by thermocouples attached to the outer surface of the cladding. More details on the experimental apparatus and conditions are given in Erbacher et al. [29] and Markiewicz and Erbacher [30].

For these cases, the BISON calculations utilize a 2D-RZ axisymmetric representation for these cladding tubes. The BISON internal coolant channel is to have an inlet temperature of 473 K with atmospheric pressure and a nearly zero mass flow rate to simulate stagnant steam. Select rod internal pressures were chosen to study within the 1–14 MPa range: 1 MPa, and all even pressures in the range from 2 to 14 MPa. Only the 1 K/s cases were analyzed here. A slight axial profile was applied to the interior surface to induce localized ballooning. Different simulations were completed using two of the different high-temperature creep models, Erbacher and Donaldson, in addition to the three different burst opening area models were studied. A combined overstress and plastic instability failure criterion was used. Details of the failure criterion can be found in the BISON documentation [31].

4.1.1.1 Burst Temperature

The burst temperature correlates with the time to burst. Figure 4.1 presents the burst temperature as a function of the internal overpressure for both the Erbacher and Donaldson high-temperature creep models. At low overpressures, the two creep models compute similar burst temperatures. At high overpressures, the

Donaldson model more accurately captures the rupture temperature when compared to the experimental data. Previous work [2] showed that the addition of anisotropy to the Erbacher creep model resulted in an increase in the rupture temperature for a certain overpressure as well. Future work is to combine the Hill anisotropic approach presented in Reference [32] with the new high-temperature creep models.

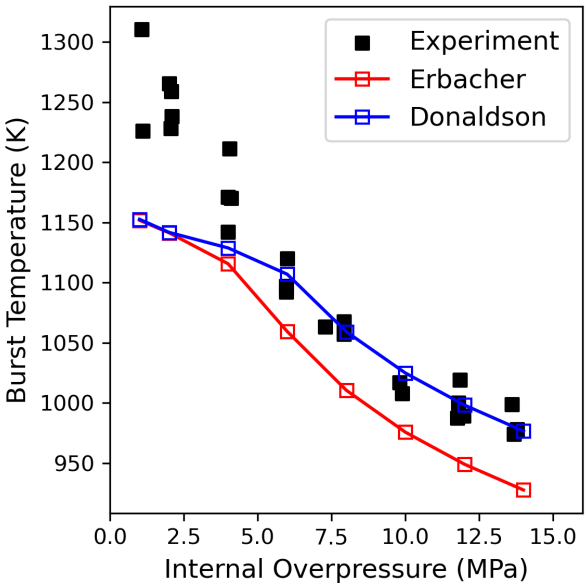

Figure 4.1. Computed rupture temperatures compared to the experimental measurements for the Erbacher and Donaldson creep models.

4.1.1.2 Rupture Area

The rupture area for the REBEKA experiments is not reported. However, based upon the calculations of the peak cladding hoop stress or strain (depending upon the model used), the calculated rupture area can be determined. By comparing the rupture area computed by the three different models (Jernkvist, ORNL average, and ORNL limiting), insight can be gained on the impact that the different high-temperature creep models have on the stress or strain calculations. Table 4.1 and Table 4.2 present the computed rupture area for the different combinations of creep model, rupture area model, and internal overpressure. For the ORNL model, a rupture shape of a rhombus is assumed. The key observations from the rupture area calculations for the REBEKA cases are that the Jernkvist rupture area model computes an increasingly larger rupture area as the ovepressure increases since it is based on the peak hoop stress. On the other hand, the ORNL models do not compute a rupture area until a strain over 8% is attained. For the Erbacher model, this occurs at an overpressure of 4 MPa, whereas, for the Donaldson model, this occurs at 6 MPa. For both creep models, the Jernkvist-calculated area is always bounded by the ORNL average and ORNL limiting cases when the strain is over 8%. The ORNL models begin to compute slightly smaller rupture areas as the overpressure increases due to the decrease in the peak hoop strain. At high overpressures, the rupture area is larger when the Donaldson creep model is used.

Table 4.1. Calculated rupture areas when using the Erbacher creep model.

Overpressure (MPa)	Peak Hoop Stress (MPa)	Peak Hoop Strain (%)	Jernkvist Area (mm^2)	ORNL Average Area (mm^2)	ORNL Limiting Area (mm^2)
1	5.71	0.42	0.17	0	0
2	12.3	1.24	7.1	0	0
4	35.5	20.9	33.2	12.3	68.1
6	58.2	25.4	48.0	17.5	87.4
8	76.7	24.4	54.6	16.5	83.5
10	95.0	23.8	58.2	15.7	80.7
12	113.2	23.2	60.1	15.1	78.3
14	131.2	22.7	61.2	14.5	76.4

Table 4.2. Calculated rupture areas when using the Donaldson creep model.

Overpressure (MPa)	Peak Hoop Stress (MPa)	Peak Hoop Strain (%)	Jernkvist Area (mm^2)	ORNL Average Area (mm^2)	ORNL Limiting Area (mm^2)
1	5.69	0.38	0.17	0	0
2	12.1	0.60	6.94	0	0
4	26.5	3.93	24.3	0	0
6	61.2	28.3	49.4	20.7	99.0
8	79.7	26.7	55.3	19.0	92.7
10	99.0	26.1	58.7	18.3	90.4
12	118.0	25.6	60.5	17.8	88.5
14	137.0	25.2	61.5	17.4	86.9

4.2 Integral Rod Experiments

4.2.1 Halden IFA-650 Test Series

Experiments from the Halden IFA-650 test series are some of the staple validation cases used to assess changes in FFRD- and LOCA-based models in BISON. In particular, Rods IFA-650.2, IFA-650.4, IFA-650.9, and IFA-650.10 have been extensively used, given the BISON teams participation in the FUMAC project [33]. More recently [27, 25], IFA-650.14 has been added to the validation suite to assess the impact of various model improvements on a rod that had extensive relocation but no cladding rupture. In particular, IFA-650.4 has been referred to as the experiment whose observations reignited the rapid investigation into FFRD by industry, national laboratories, and universities. This case was irradiated to a very high rod average burnup (∼92 MWd/kgU) with a single observable cladding balloon, with severe pulverization and fuel relocation. The IFA-650.9 experiment was designed to confirm the observations from IFA-650.4 on high-burnup fuel. This rod was irradiated to a slightly lower rod average burnup of ∼89.9 MWd/kgU, with a unique double cladding balloon, severe pulverization, and fuel relocation. As mentioned previously, IFA-650.14 was designed with a very small plenum to induce large balloons, moderate pulverization, and fuel relocation but no cladding rupture. The burnup of this rod was ∼70.9 MWd/kgU. The other two rods analyzed with BISON in the test series focused on the cladding distension and prediction of balloon characteristics. The temperature-dependent emissivity model described in Chapter 2 is active during the post-blowdown phase of the IFA-650.4, IFA-650.9, and IFA-650.14 analyses.

The simulations performed with BISON explore the impact of a new pulverization threshold and the Donaldson high-temperature creep model on the results. In all cases, the failure criterion was a strain-rate-based criterion that terminates the simulation when the cladding creep strain rate exceeds 2.77×10^{-2} s^{-1}. For IFA-650.2 and IFA-650.10, the focus was on the cladding ballooning behavior due to the high-temperature creep model change from Erbacher to Donaldson. Figure 4.2 presents the comparison of the cladding outer diameter from both the Erbacher and Donaldson creep models to the experimental measurements. The main observation in both cases is that the Donaldson creep model predicts a smaller cladding outer diameter than Erbacher under these conditions. A shift in the axial location of the peak cladding diameter in the BISON simulations towards the rupture area can be obtained by including anisotropic creep, as presented previously [2]. Combining the new high-temperature creep models and an anisotropic treatment will improve the results further and is the subject of future work.

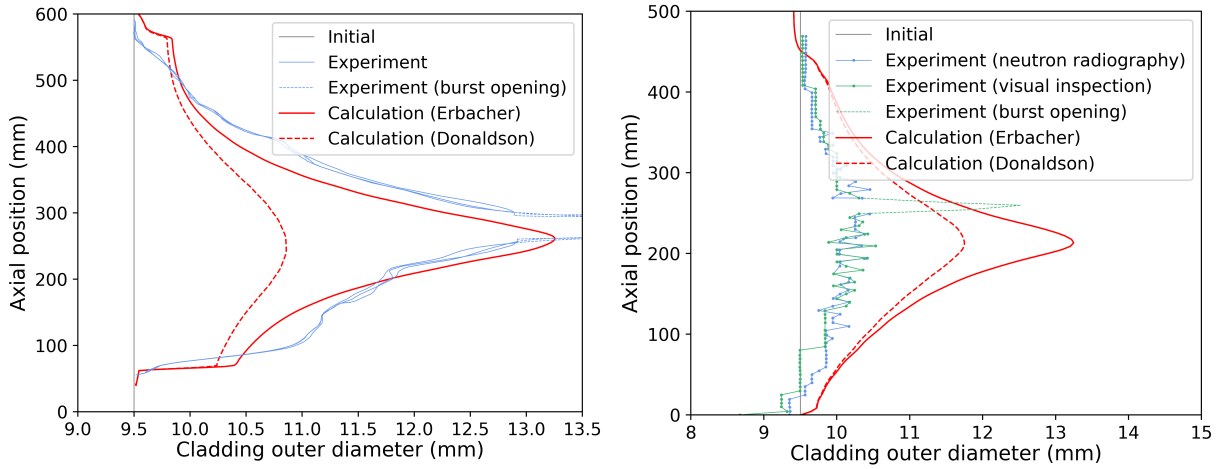

(a) (b)

Figure 4.2. Comparisons of BISON calculations for the cladding outer diameter using the Erbacher and Donaldson high-temperature creep models for (a) IFA-650.2 and (b) IFA-650.10.

Figure 4.3 presents the fuel mass fraction as a function of axial position computed by BISON for the IFA-650.4, IFA-650.9, and IFA-650.14 rods. The results for are evaluated using six different scenarios in regards to the pulverization threshold model: the `analytical`, `no_updates`, `evolve_bubble_pressure`, `fracture_criterion_3D`, `both_updates`, and `both_updates_donaldson`. These correspond to the use of the analytical threshold, the 2D fracture model with the bubble evolution model turned off, the 2D fracture model with the bubble evolution model turned on, the 3D fracture model with the bubble evolution model turned off, the 3D fracture model with the bubble evolution model turned on, and the 3D fracture model with the bubble evolution model turned on, as well as the use of the Donaldson model for high-temperature creep, respectively. For the most part, the results are qualitatively the same for IFA-650.4 and IFA-650.9, except for the analysis using the Donaldson high-temperature creep model. For IFA-650.4, the amount of fuel movement is suppressed in when the bubble pressure evolution model is activated. A smaller suppression is observed when the 3D fracture criterion is used. It is expected that both of the new additions to the pulverization threshold will reduce pulverization. A reduction in pulverization will result in less fuel movement unless the cladding diameter is large enough to permit the movement of larger fuel fragments. In the case of IFA-650.9, where the heat transfer coefficient during the post blowdown phase varies axially, it is observed that, by using the Donaldson creep model, there is a large increase in fuel movement. Given the different nature

of the creep correlation, the creep rate is lower but the simulation terminates at a later time. The larger balloons will permit the movement of large fuel fragments even if pulverization was not computed for the Donaldson case due to both the bubble pressure evolution and 3D fracture criterion models being active. The IFA-650.14 experiment containing the small plenum observed significantly different behavior than the previous two rods. This is because the experiment was designed to induce large cladding strains without failure and to promote the relocation of large fuel particles. The thermal-hydraulic loading conditions for this case are similar to those of IFA-650.2 and IFA-650.10, which results in a reduction in the fuel movement when using the Donaldson model. Additional work is necessary to gain an improved understanding of how the pulverization threshold criteria impact the fuel relocation as well as the prediction of the amount of fuel pulverized, considering that these rods experimental observed severe fine fragmentation and that the inclusion of the bubble evolution model effectively prevents pulverization from occurring.

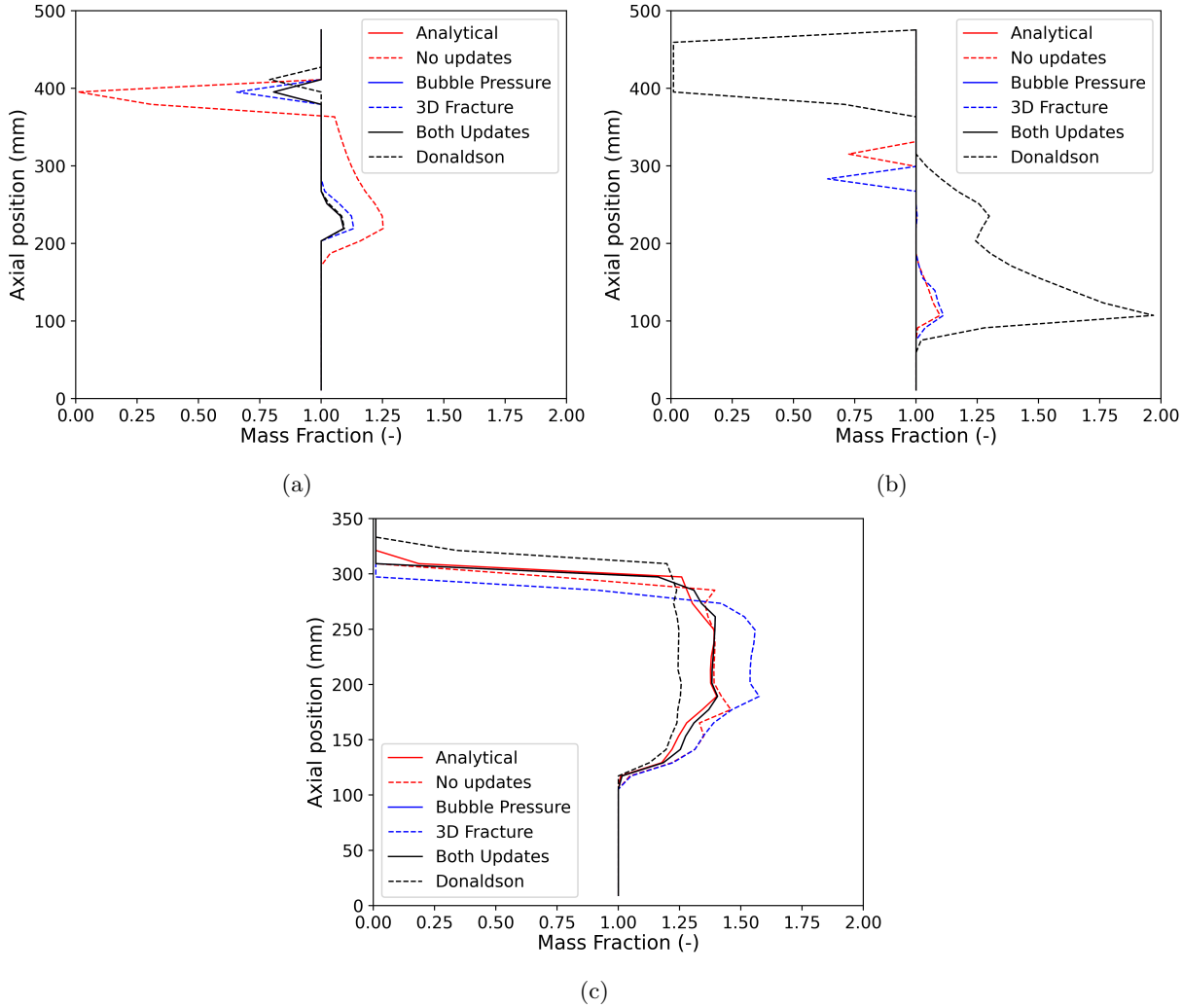

Figure 4.3. Comparisons of BISON calculations for the mass fraction when using all of the different combinations available for the pulverization threshold for (a) IFA-650.4, (b) IFA-650.9, and (c) IFA-650.14.

A preliminary transient fission gas release model was presented in Section 2.2. It was highlighted that, since the tFGR only accounts for the FGR resulting from pulverization, pulverization must occur for tFGR to be possible. In the IFA-650 Halden test series, the measurement of gas released during the transient was not one of the experimental metrics of interest. However, a recent research information letter [34] has identified tFGR as a critical component to understanding fuel rod behavior under LOCA. Some data is provided in the research information letter, but it does not identify from which experiments the data was obtained or measured. Therefore, we wanted to assess how much tFGR is calculated based upon the model in its current state. Table 4.3– Table 4.5 show the base FGR, transient FGR, and total FGR for the IFA-650.4, IFA-650.9, and IFA-650.14 rods. The `no_updates` and `fracture_criterion_3D` cases were the only ones to compute observable pulverization and therefore were the only ones to predict additional fission gas to be released during the transient. For the IFA-650.9 simulations, the tFGR predicted in those two cases was significant, with approximately twice the predicted amount of gas released compared to calculations made without the tFGR contribution. This is attributed to the large pulverized volume predicted in the `no_updates` and `fracture_criterion_3D` cases.

Table 4.3. BISON fission gas release results for IFA-650.4

Case	Base FGR (mol)	Transient FGR (mol)	Total FGR (%)
no_updates	1.09×10^{-3}	7.4×10^{-4}	5.98
evolve_bubble_pressure	1.09×10^{-3}	0	3.56
fracture_criterion_3D	1.09×10^{-3}	1.15×10^{-4}	3.93
both_updates	1.09×10^{-3}	0	3.56
both_updates_donaldson	1.09×10^{-3}	0	3.56

Table 4.4. BISON fission gas release results for IFA-650.9

Case	Base FGR (mol)	Transient FGR (mol)	Total FGR (%)
no_updates	1.92×10^{-3}	1.75×10^{-3}	10.97
evolve_bubble_pressure	1.92×10^{-3}	0	5.73
fracture_criterion_3D	1.92×10^{-3}	1.27×10^{-3}	9.52
both_updates	1.92×10^{-3}	0	5.73
both_updates_donaldson	1.92×10^{-3}	0	5.73

Table 4.5. BISON fission gas release results for IFA-650.14

Case	Base FGR (mol)	Transient FGR (mol)	Total FGR (%)
no_updates	1.30×10^{-4}	8.52×10^{-5}	1.49
evolve_bubble_pressure	1.30×10^{-4}	0	0.90
fracture_criterion_3D	1.31×10^{-4}	5.11×10^{-5}	1.26
both_updates	1.30×10^{-4}	0	0.90
both_updates_donaldson	1.30×10^{-4}	0	0.90

4.2.2 Studsvik LOCA Tests

BISON has been used to simulate Rods 191 and 196 from the Nuclear Regulatory Commission–sponsored LOCA tests in previous years [2]. These rods were originally selected because Rod 191 experienced severe fine fragmentation and relocation, while Rod 196 did not. This year, two additional rods from the test series (Rods 192 and 193) have been added to have additional cases available to explore the effects of the new pulverization threshold changes as well as the new high-temperature creep models. Details of the BISON setup for Rods 191 and 196 have been presented elsewhere [2, 25] and are omitted here for brevity. Details of the experimental apparatus and conditions are provided in References [35, 36]. Both Rods 192 and 193 have similar setup to Rod 191. Rod 193 is from the same commercial assembly as Rod 191, and therefore the base irradiation is assumed to be the same. The peak cladding temperature during the transient is also identical to Rod 191 (1443 K). The primary difference between Rod 191 and 193 is the refabrication pressure being 8.2 MPa instead of 11 MPa. Rod 192 on the other hand has a similar discharge burnup as Rod 191 and the same peak cladding temperature and refabrication pressure. However, this rod is from a different commercial assembly for which the base irradiation is unknown. To achieve the known discharge burnup, a simple base irradiation is supplied where the power is ramped up to 20 kW/m and held until a rod average burnup of ∼72 MWd/kgU is attained. This corresponds to approximately 4.75 years of irradiation.

Two main metrics of interest are analyzed in this work for the Studsvik rods, the mass of pulverized fuel released during the LOCA and the amount of transient fission gas release. Here, the overstrain ($\epsilon_{hoop,creep} > 0.336$) failure criterion is used as the point of cladding failure. Similarily to the IFA-650 cases, the results are evaluated using five different scenarios in regards to the pulverization threshold model. The definitions are the same as the IFA-650 cases, with the exception that the analytical model was not included for the Studsvik rods as the results from last year [2] showed that the analytical model resulted in zero pulverization.

Table 4.6– Table 4.9 presents the results of the simulations of the four Studsvik rods. The mass of pulverized fuel released during the LOCA for the BISON simulations is assumed to be any and all fuel that pulverized during the transient. Similar to the tables presented for the IFA-650 test series, the base FGR, transient FGR, and total FGR is shown. For all rods, the same trends are observed in regards to the various changes in the pulverization threshold and the associated tFGR computed. The case where the 2D fracture criterion is active and no bubble pressure evolution is employed shows a significant amount of pulverization. In Rods 191–193, this value is less than what was experimentally observed. In the low burnup Rod 196 case, the amount of pulverized fuel is more than experimentally released. Including the bubble evolution model results in a suppression of pulverization and subsequent tFGR. The results of Rod 191 and 193, as setup here (i.e., the refabrication pressure changing from 11 to 8.2 MPa), were identical. Comparing Rods 191 and 192, where the only difference is the base irradiation history (which is assumed for Rod 192 to achieve the discharge burnup), one observes slight differences in the amount of tFGR, which is attributed to the changes in the temperatures attained during normal operation (cycles in Rod 191 versus a constant power in Rod 192). It is suspected that there is a power history effect on the likelihood of pulverization as well given the fact that the use of the 3D fracture criterion results in a significant reduction in pulverized fuel for the Rod 192 case compared to Rods 191 and 193. The other main difference between Rods 191, 192, and 193 that is not accounted for in the BISON simulations is the hydrogen content.

Table 4.6. BISON simulation results for Studsvisk Rod 191, including the experimental mass released.

Case	BISON Mass Released (g)	Experiment Mass Released (g)	Base FGR (mol)	Transient FGR (mol)	Total FGR (%)
no_updates	25.4	52	8.30×10^{-5}	2.16×10^{-4}	2.6
evolve_bubble_pressure	7.0	52	8.30×10^{-5}	7.0×10^{-6}	0.782
fracture_criterion_3D	24.9	52	8.30×10^{-5}	2.11×10^{-4}	2.56
both_updates	0	52	8.30×10^{-5}	0	0.721
both_updates_donaldson	0	52	8.30×10^{-5}	0	0.721

Table 4.7. BISON simulation results for Studsvisk Rod 192, including the experimental mass released.

Case	BISON Mass Released (g)	Experiment Mass Released (g)	Base FGR (mol)	Transient FGR (mol)	Total FGR (%)
no_updates	25.4	68	1.74×10^{-4}	2.17×10^{-4}	3.13
evolve_bubble_pressure	0	68	1.74×10^{-4}	0	1.39
fracture_criterion_3D	11.3	68	1.74×10^{-4}	9.59×10^{-5}	2.16
both_updates	0	68	1.74×10^{-4}	0	1.39
both_updates_donaldson	0	68	1.74×10^{-4}	0	1.39

Table 4.8. BISON simulation results for Studsvisk Rod 193, including the experimental mass released.

Case	BISON Mass Released (g)	Experiment Mass Released (g)	Base FGR (mol)	Transient FGR (mol)	Total FGR (%)
no_updates	25.4	105	8.30×10^{-5}	2.16×10^{-4}	2.6
evolve_bubble_pressure	7.0	105	8.30×10^{-5}	7.0×10^{-6}	0.782
fracture_criterion_3D	24.9	105	8.30×10^{-5}	2.11×10^{-4}	2.56
both_updates	0	105	8.30×10^{-5}	0	0.721
both_updates_donaldson	0	105	8.30×10^{-5}	0	0.721

Table 4.9. BISON simulation results for Studsvisk Rod 196, including the experimental mass released.

Case	BISON Mass Released (g)	Experiment Mass Released (g)	Base FGR (mol)	Transient FGR (mol)	Total FGR (%)
no_updates	22.8	0	1.74×10^{-4}	1.925×10^{-4}	4.03
evolve_bubble_pressure	0	0	1.74×10^{-4}	0	1.92
fracture_criterion_3D	22.8	0	1.74×10^{-4}	1.925×10^{-4}	4.03
both_updates	0	0	1.74×10^{-4}	0	1.92
both_updates_donaldson	0	0	1.74×10^{-4}	0	1.92

5. Conclusions and Future Work

This report summarizes the Fiscal Year 2022 advancements in mechanistic and empirical modeling with the BISON fuel performance code in relation to FFRD and LOCA phenomenon. Multiple new capabilities have been added and existing capabilities have been enhanced to support more rigorous analyses. These changes include an updated LLS-informed pulverization threshold, a preliminary transient fission gas release model, two new high-temperature Zircaloy creep models, an extension of the existing hydrogen embrittlement and damage model to work with creep models, two empirical cladding rupture area models, and a temperature-dependent emissivity for radiation model. Mesoscale work has also been initiated in implementing a new LLS-informed recrystallization fraction model. Details of this new recrystallization model was presented in Section 2.3. These new models were then verified to be properly implemented in the code through the use of implementation testing. Next, the cladding rupture area, Donaldson high-temperature creep model, pulverization threshold, and tFGR model were assessed against a suite of separate effects and integral rods tests. The assessment highlighted that the inclusion of the bubble pressure evolution model in the pulverization threshold had the strongest impact compared to the 3D fracture criterion on reducing the amount of fuel predicted to have pulverized. In some cases, pulverization was precluded completely. The 3D fracture criterion has a much smaller impact on reducing pulverization. The empirical rupture area models showed consistent results in the sense that the Jernkvist model was bounded by the ORNL average and limiting models when the peak cladding hoop strain was high enough for the ORNL models to calculate an area.

Future work is necessary in a multitude of areas to understand why the existing mechanistic and empirical models for FFRD and LOCA are behaving as they are. In addition, improvements have been identified that can further the predictive capability of some of the models.

1. The completion of the mesoscale-informed recrystallization fraction model is necessary.
2. The extension of the preliminary tFGR model to consider variable fragment shapes and sizes beyond a cuboid of fixed size is necessary.
3. An investigation into the convergence behaviors of the Kaddour high-temperature creep model on assessment cases is required. Despite the model testing yielding realistic stress contours, convergence on integral and separate effects experiments was nonexistent. The difficulties are likely related to the change in creep rate at the 15 MPa stress transition in the alpha phase, but more work is needed.
4. Additional case studies are needed for when the hydrogen embrittlement and damage model is included in a LOCA analysis. Currently, the model expects the hydride content and orientation to input to the model, which is typically not known from the experiment. Coupling to the Hydrogen, Nucleation, Growth, and Dissolution model [37, 38, 39] available in BISON would be necessary for a more rigorous analysis.

Acknowledgments

This report was authored by a contractor of the U.S. Government under contract DE-AC07-05ID14517. Accordingly, the U.S. Government retains a non-exclusive, royalty-free license to publish or reproduce the published form of this report, or allow others to do so, for U.S. Government purposes. Funding was provided by the Nuclear Energy Advanced Modeling and Simulation program.

This research made use of the resources of the High Performance Computing Center at Idaho National Laboratory, which is supported by the DOE Office of Nuclear Energy and the Nuclear Science User Facilities under contract no. DE-AC07-05ID14517.

Bibliography

[1] Richard L. Williamson et al. "BISON: A Flexible Code for Advanced Simulation of the Performance of Multiple Nuclear Fuel Forms". In: *Nuclear Technology* 207.7 (2021), pp. 954–980. DOI: 10.1080/00295450.2020.1836940.

[2] K. A. Gamble et al. *Advancements in modeling fuel pulverization and cladding behavior during a LOCA*. Tech. rep. INL/EXT-21-64705. Idaho National Laboratory, 2021.

[3] D. R. Olander. *RIA-related issues concerning fission gas in irradiated PWR fuel*. Tech. rep. Institut de Protection et de Surete Nucleaire, Cadarache, France, 1997.

[4] K. Kulacsy. "Mechanistic model for the fragmentation of the high-burnup structure during LOCA". In: *Journal of Nuclear Materials* 466 (2015), pp. 409–416.

[5] Larry K Aagesen et al. *Mesoscale simulations to inform microstructure-based pulverization criterion in high-burnup UO_2*. Tech. rep. INL/EXT-21-64275 Rev. 0. Idaho National Laboratory, 2021.

[6] Larry K Aagesen et al. *Implementation and testing of physics-based pulverization model in BISON*. Tech. rep. INL/RPT-22-67941 Rev. 0. Idaho National Laboratory, 2022.

[7] T. Barani et al. "Multiscale modeling of fission gas behavior in U3Si2 under LWR conditions". In: *Journal of Nuclear Materials* 522 (2019), pp. 97 –110. ISSN: 0022-3115. DOI: 10.1016/j.jnucmat.2019.04.037.

[8] D. R. Olander. *Fundamental aspects of nuclear reactor fuel elements*. Technical Information Center, Energy Research and Development Administration, 1976.

[9] Katsumi Une, Shinji Kashibe, and Akira Takagi. "Fission Gas Release Behavior from High Burnup UO2 Fuels under Rapid Heating Conditions". In: *https://doi.org/10.1080/18811248.2006.9711208* 43 (9 2006), pp. 1161–1171. ISSN: 00223131. DOI: 10.1080/18811248.2006.9711208. URL: https://www.tandfonline.com/doi/abs/10.1080/18811248.2006.9711208.

[10] J. P. Hiernaut et al. "Fission product release and microstructure changes during laboratory annealing of a very high burn-up fuel specimen". In: *Journal of Nuclear Materials* 377 (2 July 2008), pp. 313–324. ISSN: 0022-3115. DOI: 10.1016/J.JNUCMAT.2008.03.006.

[11] J. Spino et al. "Stereological evolution of the rim structure in PWR-fuels at prolonged irradiation: Dependencies with burn-up and temperature". In: *Journal of Nuclear Materials* 354 (1-3 Aug. 2006), pp. 66–84. ISSN: 0022-3115. DOI: 10.1016/J.JNUCMAT.2006.02.095.

[12] F. Cappia et al. "Critical assessment of the pore size distribution in the rim region of high burnup UO2 fuels". In: *Journal of Nuclear Materials* 480 (Nov. 2016), pp. 138–149. ISSN: 0022-3115. DOI: 10.1016/J.JNUCMAT.2016.08.010.

[13] Tommaso Barani et al. "Modeling high burnup structure in oxide fuels for application to fuel performance codes. Part II: Porosity evolution". In: *Journal of Nuclear Materials* 563 (May 2022), p. 153627. ISSN: 0022-3115. DOI: 10.1016/J.JNUCMAT.2022.153627.

[14] Katsumi Une, Shinji Kashibe, and Kimio Hayashi. "Fission Gas Release Behavior in High Burnup UO2 Fuels with Developed Rim Structure". In: *https://doi.org/10.1080/00223131.2002.10875557* 39 (2002), pp. 668–674. ISSN: 00223131. DOI: 10.1080/00223131.2002.10875557. URL: https://www.tandfonline.com/doi/abs/10.1080/00223131.2002.10875557.

[15] M. Marcet et al. "In situ Characterization of UO2 Microstructure Changes During an Annealing Test in an Environmental Scanning Electron Microscope". In: *MRS Online Proceedings Library (OPL)* 1215 (2009), pp. 157–162. ISSN: 0272-9172. DOI: 10.1557/PROC-1215-V16-44. URL: https://www.cambridge.org/core/journals/mrs-online-proceedings-library-archive/article/abs/in-situ-characterization-of-uo2-microstructure-changes-during-an-annealing-test-in-an-environmental-scanning-electron-microscope/A13516F89AE0A076C6D9E2721040ABAD.

[16] M. Marcet et al. "High Burn up Structure Contribution to the Fission Gas Release under Transient Conditions". In: Sept. 2009, p. 268.

[17] L Aagesen et al. *Determine Fragmentation Criteria in High-burnup UO_2 Fuel during Accident Conditions*. Tech. rep. INL/EXT-20 0- Rev. 0. Idaho National Lab., Idaho Falls, ID United States, 2020.

[18] M. W. D. Cooper et al. "Multi-Scale Modeling of High Burnup Fuel Attributes Contributing to Thermally-Induced Fragmentation". In: *Top Fuel* (2021).

[19] Zehua Ma et al. "Numerical investigation of ballooning and burst for chromium coated zircaloy cladding". In: *Nuclear Engineering and Design* 383 (2021). DOI: https://doi.org/10.1016/j.nucengdes.2021.111420.

[20] A.R. Massih. *An evaluation of high-temperature creep of zirconium alloys: data versus models*. Tech. rep. SSM 2014:20. Quantum Technologies AB, 2014.

[21] D. Kaddour et al. "Experimental determination of creep properties of Zirconium alloys together with phase transformation". In: *Scripta Materialia* 51.6 (2004), pp. 515–519.

[22] A.T. Donaldson, T. Healey, and R.A.L. Horwood. *Biaxial creep deformation of Zircaloy-4 PWR fuel cladding in the alpha,(alpha + beta) and beta phase temperature ranges*. Tech. rep. British Nuclear Energy Society, 1985.

[23] L. O. Jernkvist. *Cladding tube rupture under LOCA: Data and models for rupture opening size*. Tech. rep. 2021:05. Swedish Radiation Safety Authority, 2021.

[24] N. Capps et al. "Engineering Assessment of UO_2 and Cladding Behavior under High Burnup LOCA Conditions". In: (Sept. 2021). DOI: 10.2172/1822042. URL: https://www.osti.gov/biblio/1822042.

[25] K. A. L. Gamble. "Mechanistic Multiphysics Modeling of Cladding Rupture in Nuclear Fuel Rods During Loss-Of-Coolant Accident Conditions". PhD thesis. University of South Carolina, 2022.

[26] J. Stuckert. *On the thermo-physical properties of Zircaloy-4 and ZrO_2 at high temperature*. Tech. rep. FZKA 6739. Kernforschungszentrum Karlsruhe, Germany, 2002.

[27] A. Toptan and K. A. Gamble. *BISON High Burnup Structure Modeling Capabilities Validated with a Selection of the Halden IFA-650 Rods*. Tech. rep. INL/EXT-20-60778. Idaho National Laboratory, 2020.

[28] M. Limbäck and T. Andersson. "A Model for Analysis of the Effect of Final Annealing on the In- and Out-of-Reactor Creep Behavior of Zircaloy Cladding". In: *Zirconium in the Nuclear Industry: Eleventh International Symposium*. ASTM STP 1295. 1996, pp. 448–468.

[29] F. J. Erbacher et al. "Burst criterion of Zircaloy fuel claddings in a loss-of-coolant accident". In: *Zirconium in the Nuclear Industry, Fifth Conference, ASTM STP 754, D.G. Franklin Ed.* American Society for Testing and Materials. 1982, pp. 271–283.

[30] M. E. Markiewicz and F.J. Erbacher. *Experiments on ballooning in pressurized and transiently heated Zircaloy-4 tubes*. Tech. rep. KfK 4343. Kernforschungszentrum Karlsruhe, Germany: Kernforschungszentrum Karlsruhe GmbH (Germany, 1988.

[31] Computational Mechanics and Materials Department Idaho National Laboratory. *BISON: A Finite Element-Based Nuclear Fuel Performance Code*. `https://mooseframework.inl.gov/bison/`.

[32] Recuero A., Schwen D., and Biswas S. *M3 Milestone: Anisotropic Inelastic Deformation*. Tech. rep. INL/EXT-21-62011 Rev. 1. Idaho National Laboratory, 2021.

[33] International Atomic Energy Agency. *Fuel Modeling in Accident Conditions (FUMAC) Final: Final Report of a Coordinated Research Project*. Tech. rep. IAEA-TECDOC-1889. International Atomic Energy Agency, 2019.

[34] M. Bales et al. *Interpretation of Research on Fuel Fragmentation, Relocation, and Dispersal at High Burnup*. Tech. rep. RIL 2021-13. United States Nuclear Regulatory Commission, 2021.

[35] M. Flanagan and P. Askeljung. "Observations of Fuel Fragmentation, Mobility and Release in Integral High-Burnup, Fueled LOCA Tests". In: *Enlarged Halden Program Group Meeting 2011*. 2011.

[36] M. Helin and J. Flygare. *NRC LOCA tests at Studsvik, Design and construction of test train device and tests with unirradiated cladding material*. Tech. rep. STUDSVIK/N-11/130. Studsvik, 2012.

[37] Evrard Lacroix et al. "Zirconium Hydride Precipitation and Dissolution Kinetics in Zirconium Alloys". In: *Zirconium in the Nuclear Industry: 19th International Symposium* (July 2021), pp. 67–91.

[38] Florian Passelaigue et al. "Implementation and Validation of the Hydride Nucleation-Growth-Dissolution (HNGD) model in BISON". In: *Journal of Nuclear Materials* 544 (Feb. 2021), p. 152683. ISSN: 0022-3115.

[39] Florian Passelaigue, Pierre-Clément A. Simon, and Arthur T. Motta. "Predicting the hydride rim by improving the solubility limits in the Hydride Nucleation-Growth-Dissolution (HNGD) model". In: *Journal of Nuclear Materials* 558 (Jan. 2022), p. 153363. ISSN: 0022-3115.